Nanoscale

ROYAL SOCIETY OF CHEMISTRY

PAPER

View Article Online
View Journal | View Issue

Cite this: *Nanoscale*, 2024, **16**, 18056

Zn-doped $NiMoO_4$ enhances the performance of electrode materials in aqueous rechargeable NiZn batteries†

Xingyan Zhang * and Dag Noréus

Received 8th July 2024,
Accepted 29th August 2024

DOI: 10.1039/d4nr02822h

rsc.li/nanoscale

In this work, zinc was introduced to prepare $Ni_{1-x}Zn_xMoO_4$ ($0 \leq x \leq 1$) nanoflake electrodes to increase the energy density and improve the cycling stability for a wider range of applications of aqueous rechargeable nickel–zinc (NiZn) batteries. This was achieved using a facile hydrothermal method followed by thermal annealing, which can be easily scaled up for mass production. Owing to the unique nanoflake structures, improved conductivity, and tunable electronic interaction, excellent electrochemical performance with high specific capacitance and reliable cycling stability can be achieved. When the Zn doping is 25%, the $Ni_{0.75}Zn_{0.25}MoO_4$ nanoflake electrode displays a high specific capacitance of 345.84 mA h g^{-1} (2490 F g^{-1}) at a current density of 1 A g^{-1} and improved cycling stability at a high current density of 10 A g^{-1}. NiZn cells assembled with $Ni_{0.75}Zn_{0.25}MoO_4$ nanoflake electrodes and zinc electrodes have a maximum specific capacity of 344.7 mA h g^{-1} and an energy density of 942.53 W h kg^{-1}. This design strategy for nickel-based electrode materials enables high-performance energy storage and opens up more possibilities for other battery systems in the future.

1. Introduction

Batteries have attracted increasing attention from researchers in both academia and industry owing to their rapid development into diverse products ranging from consumer electronics to grid-scale energy storage devices.[1–3] Nickel-based aqueous rechargeable batteries such as NiCd, NiMH, NiFe, and NiZn have gained renewed interest owing to their improved power density, high safety, and low cost.[4–6] Among these candidates, the rechargeable alkaline NiZn battery with its higher cell voltage has the advantages of greater energy density and higher power density and can thus be more cost-effective.[7,8] Zinc anodes have low redox potential and high theoretical capacity, and they can be safely used in a highly conductive aqueous electrolyte, making them promising for large-scale applications.[9] However, the present commercial Ni-based electrode, with its unavoidable oxygen evolution side reaction, poor conductivity, and low actual energy density, needs to be improved to better achieve the advantages of NiZn batteries.[10] Such development and improvement of nickel-based electrode materials will also be beneficial for the other Ni-based battery chemistries.

Nickel-based nanomaterials have been widely explored based on the rechargeable redox reaction between the nickel hydroxide redox couples ($Ni(II)(OH)_2/Ni(III)OOH$). They are the first choice for Ni-based batteries in industrial production. They have also received increasing attention owing to their relatively high theoretical specific capacitance of 2082 F g^{-1} and fast redox kinetics.[11,12] Nevertheless, it can be improved by developing other Ni-based redox couples. Nickel oxide (NiO) is a green crystalline solid material and a promising electrode material owing to its unique electrical properties, with excellent ion storage kinetics and a relatively high capacitance of 2573 F g^{-1}. To obtain NiO nanomaterials, some different approaches have been investigated with tunable composition, size, morphology, and crystalline structure.[13–15] Recently, nickel molybdate ($NiMoO_4$) has been recognized as a strong candidate owing to its high theoretical specific capacitance >3000 F g^{-1}. The relatively high electrochemical activity arises from the reversible redox reaction of Ni^{2+}/Ni^{3+} and the spinel crystal structure offering effective charge storage and high ion diffusion rate in a robust host structure with a three-dimensional network of well-connected interstitial sites.[16–19] It is, however, still a challenge to improve the electrochemical performance of these nanomaterials.

To improve the performance, hybrid nanostructures fabricated by combining Ni-based materials with other high-con-

Inorganic and Structural Chemistry, Department of Materials and Environmental Chemistry, Stockholm University, SE 106 91 Stockholm, Sweden.
E-mail: xingyan.zhang@mmk.su.se

† Electronic supplementary information (ESI) available. See DOI: https://doi.org/10.1039/d4nr02822h

ductive materials or conductive substrates were employed to enhance electrochemical performances.[20,21] Considerable efforts have been invested in composite strategies for these materials. Although good performance was indeed achieved, some components were too complex to analyze the mechanisms in detail, making further practical development difficult. Therefore, the introduction of heteroatoms (such as Co, Al, Zn, Mn, and Mg) was explored to understand the composition, phase transition, defects, and electronic structures to further guide the synthesis and control of the materials.[22–25] Many studies on metal ion doping have been reported to enhance the structure stability and promote the electrochemical performance of these electrode materials for Ni/Zn batteries. Fu *et al.* prepared $Ni/SnS_2@Ni(OH)_2$ decorated on carbon cloth by doping Ni to increase electro-active sites and enlarge the interfacial area, thus reaching a reversible specific capacitance of 2090 F g^{-1} at 1 A g^{-1}.[26] Shen *et al.* reported a novel and efficient zinc-induced phase reconstruction method to boost the electrochemical stability of cobalt–nickel double hydroxide cathode materials to improve the stability and rate capability for high-performance Ni/Zn batteries.[27] Xiang's group fabricated ultrathin $NiMn_xO_y$ nanosheets *via* a simple H_2-annealing process to form oxygen vacancies improving the areal capacity and cycling performance.[28] Xu *et al.* used nanosheets with high electrical conductivity and increased concentration of oxygen vacancies to construct hierarchical Co-doped $NiMoO_4$. $NiMoO_4$ with 15% cobalt doping assembled with a Zn electrode displayed high capacity and excellent cycle stability.[29] In addition, Zhao's group obtained Ni,Zn-codoped spinel $MgCo_2O_4$ *in situ* grown on a Co foam *via* a simple hydrothermal process, exhibiting enhanced capacitance and cycling stability.[30] There is a lot of work to prove that doping is a simple and effective way. For a Ni/Zn battery, Zn doping is a good choice to adjust the structure and composition of materials to tailor the structure and enhance the electrochemical performance by reducing the effects caused by the generated zincate in a zinc-rich environment.[31]

In this work, we synthesized $Ni_{1-x}Zn_xMoO_4$ nanoflakes by a simple hydrothermal method. The amount of Zn doping in $NiMoO_4$ was controlled by adjusting the proportion of metal ions added to the precursor solution during the synthesis process. The specific capacitance, rate capability, and cycling stability of the $Ni_{1-x}Zn_xMoO_4$ electrode are significantly better than those of the pristine $NiMoO_4$ electrode. Introducing Zn was simplified by the unique nanoflake structures. When the Zn-doping percentage is 25%, $Ni_{0.75}Zn_{0.25}MoO_4$ can achieve a high specific capacity of 345.84 mA h g^{-1} (2490 F g^{-1}) at 1 A g^{-1} and enhanced cycling capacitance retention at a high current density of 10 A g^{-1}. Furthermore, NiZn cells based on the $Ni_{1-x}Zn_xMoO_4$ nanoflake electrodes and zinc counter electrodes were constructed to explore the practical applications. The device exhibited high energy density, power density, and good cycling stability, presenting promising applications in aqueous rechargeable alkaline devices.

2. Experimental section

2.1. Synthesis of Zn-doped $NiMoO_4$

Zn-Doped $NiMoO_4$ was obtained by a simple one-step hydrothermal process. First, $(1 - x)$ mmol $Ni(NO_3)_2{\cdot}6H_2O$, x mmol $Zn(NO_3)_2{\cdot}6H_2O$, 1 mmol Na_2MoO_4, and 5 mmol urea were dissolved in 35 mL deionized (DI) water to obtain a uniform solution (where x = 0, 0.25, 0.5, 0.7, 0.75, 0.8, 0.9 and 1). Then, the homogeneous mixture was poured into a 50 mL Teflon-lined stainless steel autoclave, into which a piece of clean nickel foam had already been added, and kept at 150 °C for 6 h. Finally, the product was obtained and washed with DI water followed by drying at 60 °C overnight. For comparison, the same process was performed without the nickel foam. The samples were labeled as $Ni_{1-x}Zn_xMoO_4$, where x represents the amount of $Zn(NO_3)_2{\cdot}6H_2O$, and x = 0, 0.25, 0.5, 0.7, 0.75, 0.8, 0.9 and 1, respectively. Here, x describes the amount of Zn added during the synthesis process but does not represent the elemental content of the final product. Finally, all the products were obtained after thermal annealing at 300 °C for 2 h in air.

2.2. Material characterizations

X-ray powder diffraction patterns were recorded using an X-ray diffractometer (D8 DISCOVER, Bruker) in the range from 10° to 80°. The morphology of the samples was observed using a scanning electron microscope (SEM, JSM-7000F for binder-free materials, and Ultra 55 for powder materials) and a scanning transmission electron microscope (STEM, Themis Z, Thermo Fisher Scientific) equipped with an EDX detector. X-ray photoelectron spectrum (XPS) was recorded to analyze the elemental composition and valence state by employing a model of ESCALAB 250Xi (Thermo).

2.3. Electrochemical characterizations

The electrochemical characterizations were carried out in a three-electrode system using an electrochemical workstation (VSP300, Biologic, France). The obtained binder-free electrode, platinum wire, and Hg/HgO were used as the working, counter, and reference electrodes, respectively, in a 6 M KOH aqueous electrolyte solution. For the powder materials, the working electrode was prepared as follows: active material (80 wt%), acetylene black (10 wt%), and polyvinylidene difluoride (10 wt%, dissolved in *N*-methyl-pyrrolidone) were mixed to form a slurry. Then, the slurry was coated onto a Ni foam and dried at 120 °C under vacuum overnight to obtain the electrode.

For the electrode, the electrochemical performance was tested by cyclic voltammetry (CV, 0–0.6 V), galvanostatic charge–discharge measurements (GCD, 0–0.5 V), electrochemical impedance spectroscopy (EIS, 10^{-2}–10^5 Hz applied at the open circuit potential), and long-term cycling measurements. For the cell, the obtained electrode was assembled with a zinc electrode. The voltage range is 1.2–2.2 V for CV

and 1.2–1.9 V for GCD measurements, respectively. For the calculation of the electrode and battery capacity, the effective mass of the active electrode material was taken as the difference in mass of the nickel foam electrode before and after synthesis.

3. Results and discussion

The morphologies and structures of the obtained $Ni_{1-x}Zn_xMoO_4$ nanoflakes were characterized by scanning electron microscopy (SEM), as shown in Fig. 1. It can be noted that

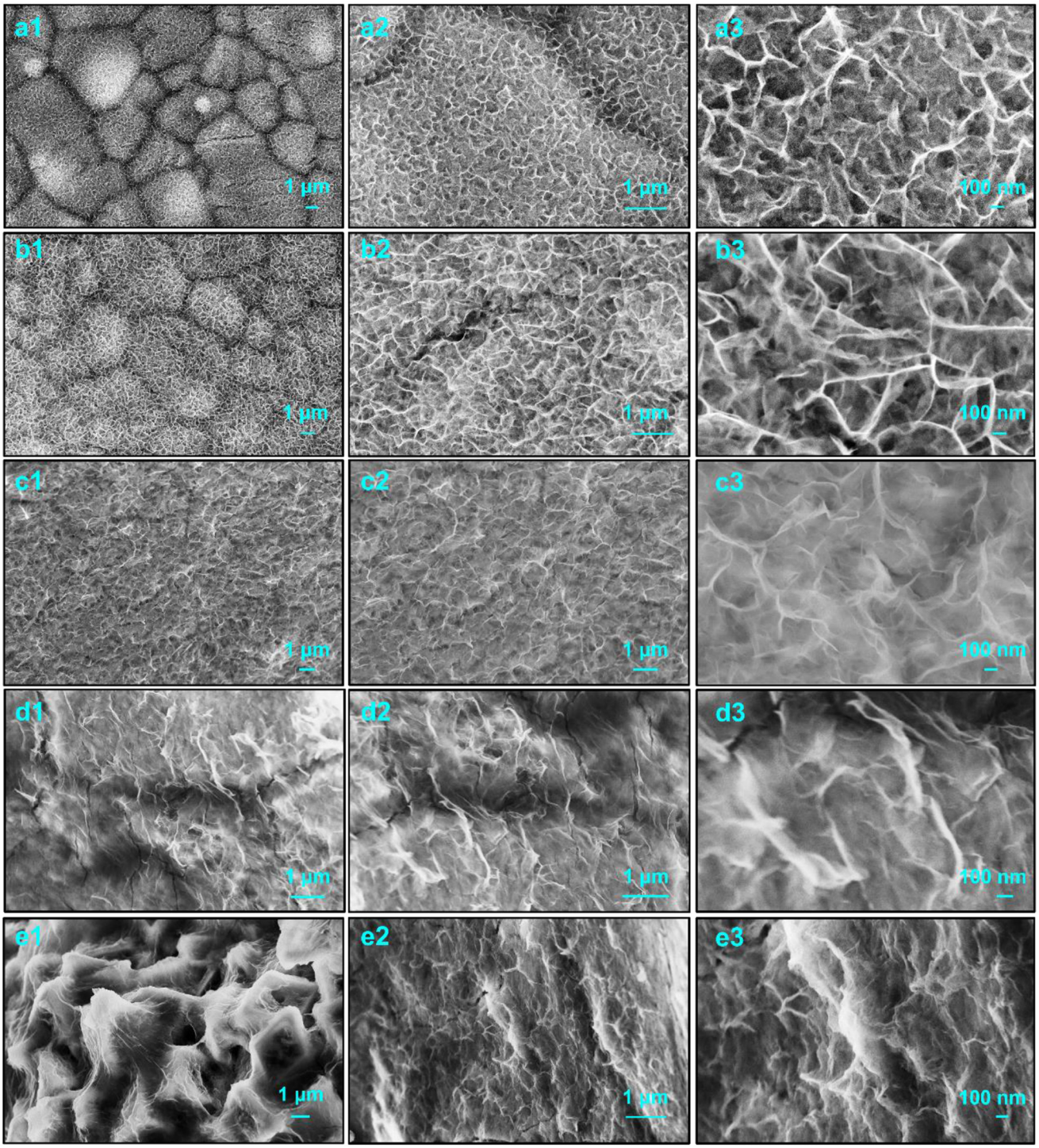

Fig. 1 SEM images of obtained materials: (a1–a3) $NiMoO_4$, (b1–b3) $Ni_{0.75}Zn_{0.25}MoO_4$, (c1–c3) $Ni_{0.5}Zn_{0.5}MoO_4$, (d1–d3) $Ni_{0.25}Zn_{0.75}MoO_4$, and (e1–e3) $ZnMoO_4$, respectively.

almost all samples exhibit a similar nanoflake structure. Generally, this special structure has a higher specific surface area and can provide more surface active sites to promote the redox reaction of the material surface layer.[32] The formation of this structure is assumed to include heterogeneous nucleation and crystal growth. In the following hydrothermal process, many ultrafine nanocrystallines are first formed on the surface of the NF substrate and become the nucleus in the subsequent growth process. Then, this nucleus adsorbs more ions and aggregates and tends to grow into small nanoflakes. Depending on the concentration of the precursor solution, material layers with different densities and thicknesses can be formed.[33] In addition, without the presence of the NF substrate, the nanoflakes will continue to serve as nucleation centers to absorb newly generated nanosheets with higher surface energy and smaller sizes. Microspheres are formed by cross-linking due to the minimizing interfacial energy, as shown in Fig. S1 (ESI†).[34]

For the obtained $Ni_{1-x}Zn_xMoO_4$ nanoflakes, Fig. 1a displays the SEM images of pristine $NiMoO_4$, in which uniform ultrathin nanoflakes can be clearly seen. Fig. 1b–d present the SEM images of obtained samples doped with different Zn contents. It can be observed that the morphologies of these samples are changed gradually. As shown in Fig. 1b, although the $Ni_{0.75}Zn_{0.25}MoO_4$ sample has a similar nanoflake structure to the pristine $NiMoO_4$ sample, the size is significantly increased and it has clearer morphological boundaries, indicating the promotion and enhancement of the structure. When the Zn content is more than 50%, the sample shows a weak nanoflake structure and a thinner layer of materials (Fig. 1c–e). Ni-Based nanoflakes are easier to form than Zn-based nanosheets owing to the presence of the nickel foam substrate. When Zn^{2+} is doped into $NiMoO_4$ to replace part of Ni^{2+}, the electronic structure of $NiMoO_4$ will be changed. The strong repulsive force between Zn and O is conducive to the transfer of electrons to Ni^{2+}, thereby enhancing the charge storage performance.[31] This indicates that the nucleation and crystallization process involves two metal cations. Their electronic structure, migration rate, ionic radius, *etc*., will affect the final morphology, crystal structure, and crystallinity, thus affecting their physical and chemical properties.

Fig. S1 (ESI†) shows the corresponding SEM images of the $Ni_{1-x}Zn_xMoO_4$ powder materials. Similarly, the pristine $NiMoO_4$ powders are microspheres with a diameter of 1–2 μm composed of numerous cross-linked nanoflakes. These microspheres have a hollow structure, clearly showing the existence of larger cavities. Their formation may be caused by the thermal decomposition and self-assembly processes of the precursor. This hollow structure can accelerate the diffusion rate and mass transfer of electrolyte ions inside the material, leading to more effective redox reactions. With the increase in Zn content, the size of the microspheres gradually increases, and the nanoflakes on the surface gradually transform into nanosheets. In partial location, the morphology looks like ultrathin nanoflakes wrapped around nanosheets. This phenomenon seems to be strengthened with the appearance of coarser and large-sized nanosheets when the Zn content reaches 50%. However, when only zinc cations were added to completely replace the nickel cations, stronger nanosheets with uniform distribution appeared. This process is basically similar to the above-mentioned growth process on the NF substrate. Furthermore, as shown in Fig. 2a, the scanning transmission electron microscopic (STEM) images confirm the ultrathin nanoflake structure of the obtained $Ni_{0.75}Zn_{0.25}MoO_4$ materials coated onto the NF. The corresponding EDX mapping and element spectrum (Fig. S2a, ESI†) illustrate the existence and uniform distribution of the Ni, Zn, Mo, and O elements, respectively.

In Fig. S2b (ESI†), the crystal structure and crystallinity of the obtained $Ni_{1-x}Zn_xMoO_4$ nanomaterials were confirmed by X-ray diffraction (XRD). As shown in Fig. S2b (ESI†), the signal of the NF substrate (JCPDS card no. 04-0850) dominates the XRD pattern.[35] Local exposure outside the NF makes the signal of the materials weak. Thus, the partially enlarged XRD patterns of the obtained materials with different Zn contents are presented to assist in analyzing the crystal phase structure (shown in Fig. S2c, ESI†). In the beginning, it was difficult to distinguish the peaks to determine the phase composition owing to their weak signal and strong noise. The peaks roughly were conjectured to be crystal planes of $NiMoO_4$ (JCPDS card no. 12-0348).[34] As Zn is added and its content increases, the peak position shifts slightly, indicating that Zn atoms replace a part of Ni atoms resulting in a change in the lattice constants due to the increase in radius. When the content of Zn exceeds 50%, it shows mixed phases containing $NiMoO_4$ and $ZnMoO_4$ (JCPDS card no. 25-1024), which indicates that Zn was successfully doped into $NiMoO_4$. However, the $Ni_0Zn_1MoO_4$ sample becomes a mixed phase containing some zinc oxide (JCPDS card no. 36-1451), which is caused by the oxidation after calcination in air. In addition, it can be noticed that the intensity of the peak gradually increases with the increase in Zn content, which indicates that doping Zn into $NiMoO_4$ can improve the crystallinity and enhance the structural stability. Although it cannot be accurately described, the specific composition of this dopant leads to better cycle life and higher specific capacity of the $Ni_{1-x}Zn_xMoO_4$ electrodes. We attribute this to the increased diffusion of the electrolyte ions into the electrode materials.

X-ray photoelectron spectroscopy (XPS) was performed to detect the elemental composition and valence states of the $Ni_{0.75}Zn_{0.25}MoO_4$ nanoflakes. The survey spectrum (Fig. S2d, ESI†) suggests the existence of Ni, Zn, Mo, and O. The $Ni_{0.75}Zn_{0.25}MoO_4$ nanoflakes contain Zn and the atomic fraction is up to 11% corresponding to 26.37% of the mass fraction, which confirms the successful doping of Zn into $NiMoO_4$. Fig. 2b–d show the high-resolution XPS spectra of Ni 2p, Zn 2p and O 1s, respectively. The Ni 2p XPS spectrum has two main binding energy peaks at 855.8 eV and 873.55 eV belonging to Ni $2p_{3/2}$ and Ni $2p_{1/2}$ core levels accompanied by corresponding satellite peaks at 861.8 eV and 879.5 eV, respectively. The binding energy gap between Ni $2p_{3/2}$ and Ni $2p_{1/2}$ is 17.75 eV, which is in good agreement with previously reported

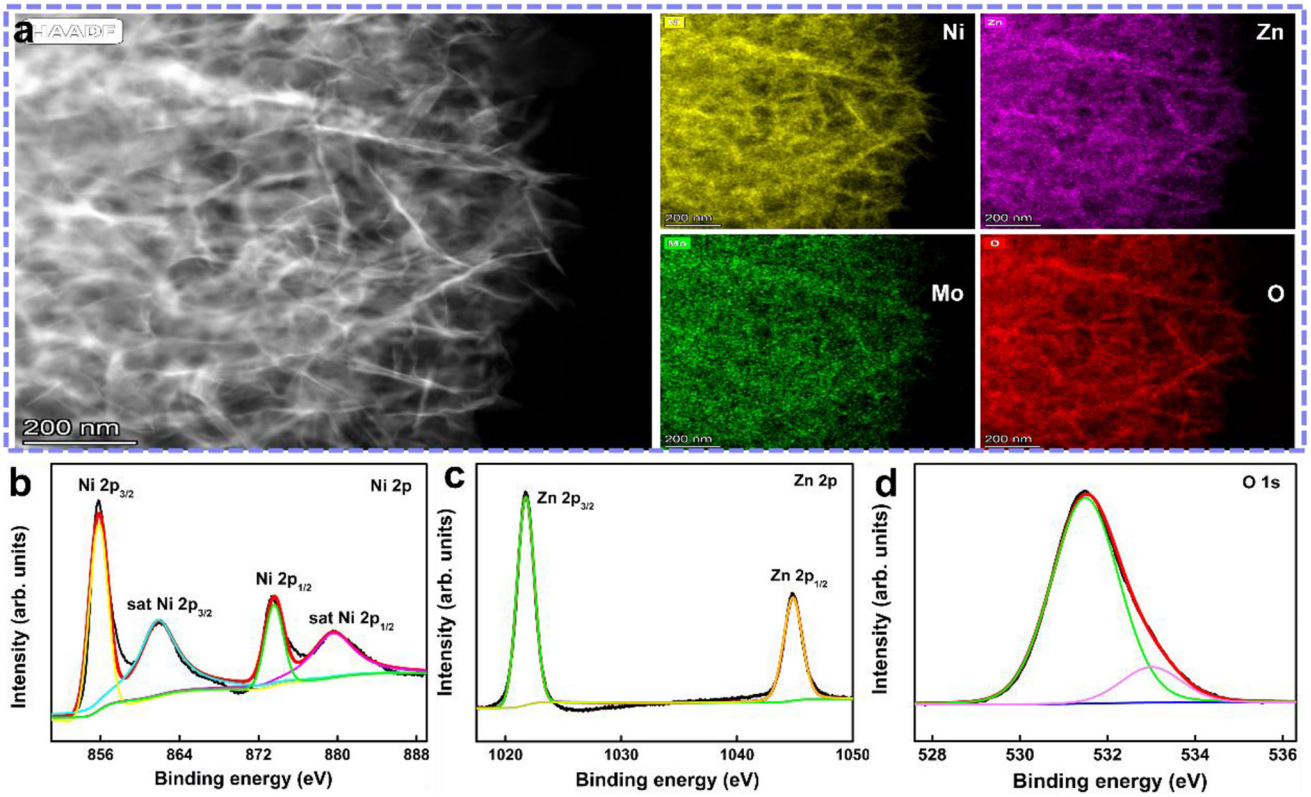

Fig. 2 (a) STEM images of $Ni_{0.75}Zn_{0.25}MoO_4$ materials and the corresponding EDX mapping, and (b–d) high-resolution XPS spectra of Ni 2p, Zn 2p, and O 1s, respectively.

data and the presence of a Ni^{2+} oxidation state.[36] The Zn 2p XPS spectrum (Fig. 2c) shows two strong peaks at 1021.76 and 1044.84 eV, corresponding to Zn $2p_{3/2}$ and Zn $2p_{1/2}$ of the Zn^{2+} state, respectively.[37] The O 1s XPS spectrum (Fig. 2d) can be composed of the lattice oxygen species at 531.49 eV and surface-adsorbed oxygen ions at 533.0 eV, which are assigned to the oxygen species in $Ni_{0.75}Zn_{0.25}MoO_4$.[38] Most importantly, it can be confirmed that the additional metal ions are successfully doped on the surface. This is probably beneficial for the electrochemical reactions that occur on the surface of the material.[31]

The $Ni_{1-x}Zn_xMoO_4$ nanomaterials were electrochemically characterized in a three-electrode system by cyclic voltammetry (CV) and galvanostatic charge–discharge (GCD) measurements. Fig. 3a compares the CV curves at 5 mV s^{-1}. All curves have a couple of peaks, revealing the reversible redox reaction in the charge/discharge process. Generally, the integral of the enclosed CV curve represents the specific capacitance. The $Ni_{0.75}Zn_{0.25}MoO_4$ electrode possesses the largest integrated area, indicating the largest specific capacitance. Additionally, Fig. 3b displays the CV curves of the $Ni_{0.75}Zn_{0.25}MoO_4$ electrode at different scan rates accompanied by broad redox peaks. This is ascribed to the reversible redox reactions between different valence states of the metal ions. First, molybdate decomposes to obtain M^{2+} metal salt ions (1); second, M^{2+} metal salt ions are converted into $M(OH)_2$ hydroxide in the alkaline electrolyte (2); finally, the faradaic redox reactions would occur between $M(OH)_2$ and MOOH as follows (3):[35,39]

$$MMoO_4 \leftrightarrow M^{2+} + MoO_4{}^{2-} \quad (1)$$

$$M^{2+} + 2OH^- \leftrightarrow M(OH)_2 \quad (2)$$

$$M(OH)_2 + OH^- \leftrightarrow MOOH + H_2O + e^- \quad (3)$$

Furthermore, the rate capability was characterized by the GCD measurement. All electrodes present similar shapes, corresponding to the redox reaction during the charge/discharge process at 1 A g^{-1}, as shown in the CV curves in Fig. 3c and S3a (ESI†). Obviously, the $Ni_{0.75}Zn_{0.25}MoO_4$ electrode has a higher capacity than other electrodes. Fig. 3d shows the GCD curves of the $Ni_{0.75}Zn_{0.25}MoO_4$ electrode at different current densities, illustrating good rate performance while maintaining a good curve shape. In Fig. 3e and S3b (ESI†), the specific capacitances of all the electrodes are compared. The specific capacities at 1 A g^{-1} of the $Ni_{1-x}Zn_xMoO_4$ (x = 0, 0.1, 0.2, 0.25, 0.3, 0.5, 0.75, and 1) electrode were calculated to be 68.88, 117.64, 182.08, 345.84, 148.43, 105.44, 54.89, and 33.38 mA h g^{-1} (495.92, 847.98, 1311.00, 2490.04, 1068.70, 759.17, 395.19, and 240.34 F g^{-1}), respectively. For the $Ni_{0.75}Zn_{0.25}MoO_4$ electrode, the specific capacitance is still 239.58 mA h g^{-1} (1724.97 F g^{-1}) at up to 10 A g^{-1}. For comparison, the CV and GCD measurements of all the powder materials are presented in

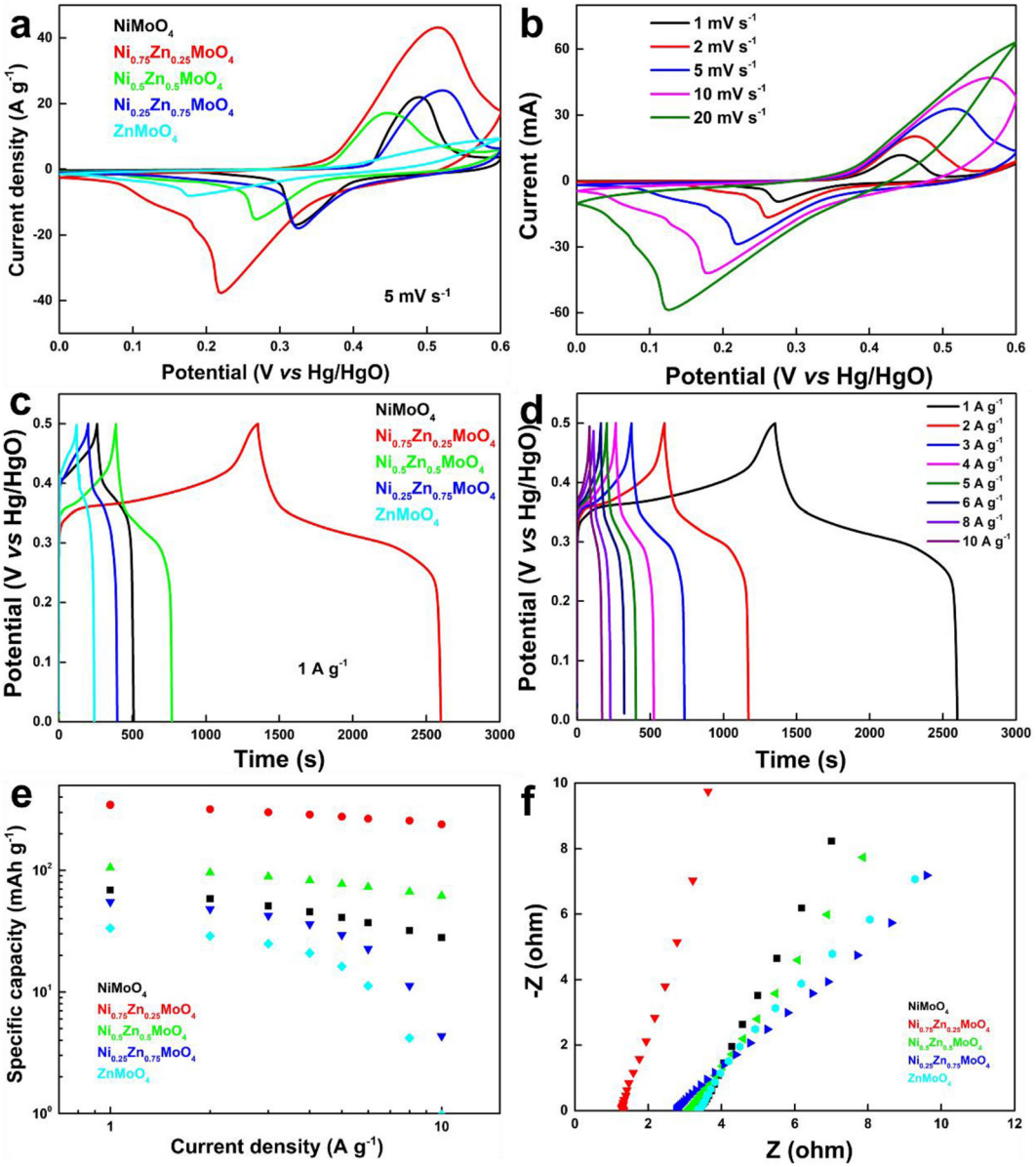

Fig. 3 Electrochemical performance in a three-electrode system (6 M KOH): (a) comparison CV curves, (b) CV curves of $Ni_{0.75}Zn_{0.25}MoO_4$, (c) comparison GCD curves, (d) GCD curves of $Ni_{0.75}Zn_{0.25}MoO_4$, (e) comparison of specific capacity at different current densities, and (f) comparison of EIS plots.

Fig. S4 (ESI†). The corresponding specific capacitances at different scan rates and current densities are plotted in Fig. S5 (ESI†). Similar electrochemical behaviors and the same trend in the above-mentioned results indicate that the design and measurements of material compositions are feasible with good stability.

The reaction kinetics of the obtained nanomaterials was evaluated by electrochemical impedance spectroscopy (EIS). All Nyquist plots have a small semicircle in the high-frequency region where the corresponding diameter is ascribed to the charge transfer resistance. As shown in Fig. 3f and S6 (ESI†), all the samples have a relatively small charge transfer resistance. A straight line in the low-frequency region reflects the ion diffusion in the bulk of the materials.[40] However, a higher slope of the Zn-doped $NiMoO_4$ electrode indicates better conductivity, when the Zn content is below 50%. This also demonstrates that the electronic structure of $NiMoO_4$ can be effectively adjusted by Zn heteroatom doping. In particular, the $Ni_{0.75}Zn_{0.25}MoO_4$ electrode exhibits the most favorable electronic conductivity, best reaction kinetics, and fast ion diffusion, probably caused by the optimized composition and cross-linked nanoflake structure.

To explore the electrochemical reaction kinetics of the $Ni_{0.75}Zn_{0.25}MoO_4$ electrode, the capacitance contribution was evaluated from the CV curves between 0.2 and 1 mV s^{-1}. Weak polarization with a slight shifting of redox peaks at low scan

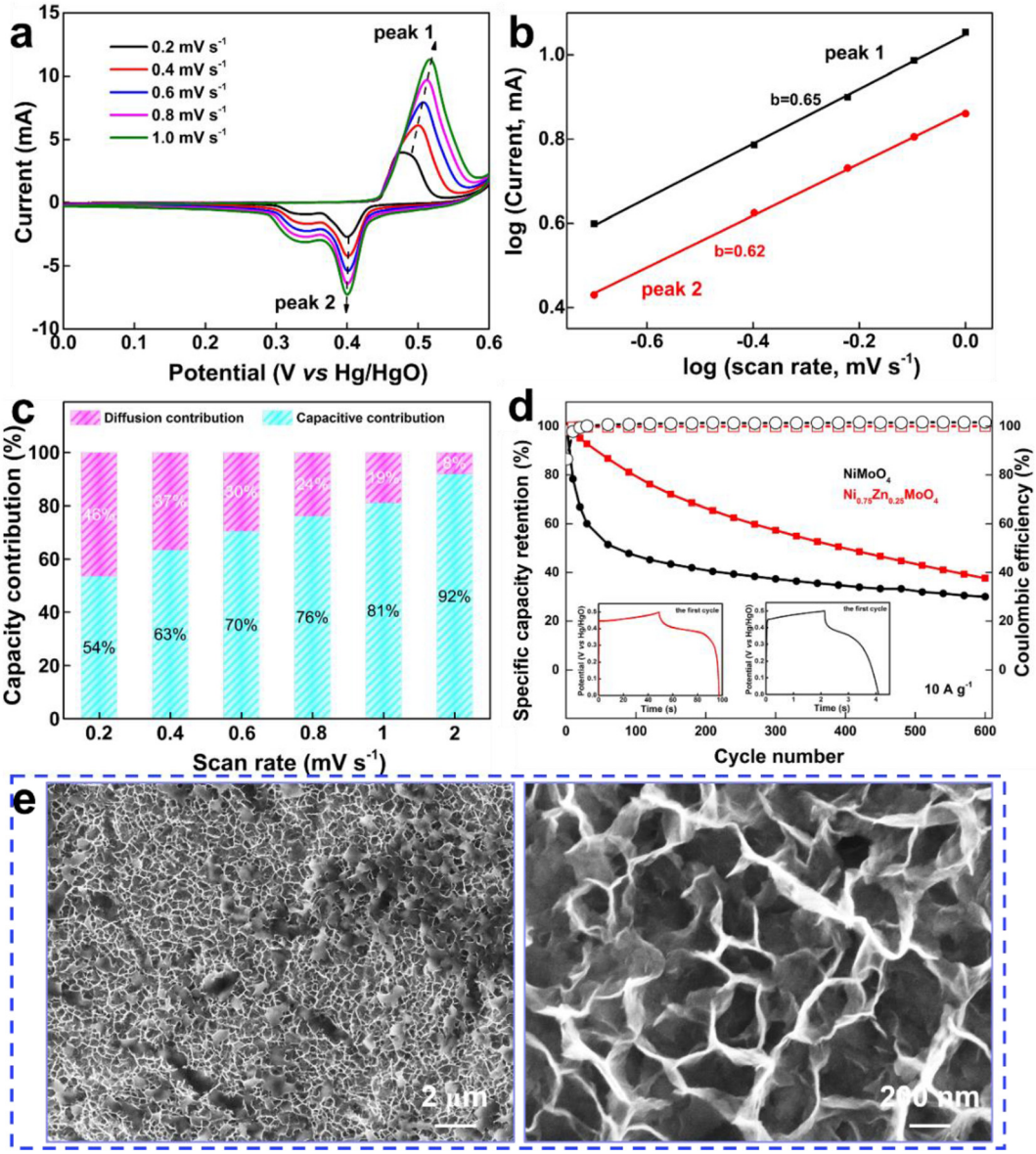

Fig. 4 (a) CV curves, (b) relationship between log(scan rate) and log(current), (c) percentages of capacity distribution at different scan rates of the obtained $Ni_{0.75}Zn_{0.25}MoO_4$ electrode in a 6 M KOH electrolyte, (d) comparison of cycling stability at 10 A g^{-1}, the insets are the GCD curves before cycling, and (e) SEM images after cycling.

rates is shown in Fig. 4a. In general, this capacitance contribution can be evaluated by $i = av^b$, i is the current, v is the scan rate, and a and b are adjustable constants.[41] Therefore, the b value which is calculated by the slope of $\log(i) = b\log(v)$ defines the charge storage process. When b is close to 0.5, the capacitance is dominated by ionic diffusion which is a slow faradaic process; when b is close to 1, the capacitance is distributed by the fast surface-scale redox reaction and the adsorption of the electrolyte ions. Based on the results in Fig. 4a, the values of b corresponding to cathodic and anodic peaks were calculated to be 0.65 and 0.62 (Fig. 4b), respectively, which indicates that the electrochemical kinetics of the $Ni_{0.75}Zn_{0.25}MoO_4$ electrode includes both diffusion and surface scale processes.

To further investigate the charge storage mechanism, Dunn's equation ($i(V) = k_1v + k_2v^{1/2}$, where $i(V)$ is the peak current, and k_1 and k_2 are adjustable constants) was employed for distinguishing the ratio of the capacitance contribution. Here, k_1v and $k_2v^{1/2}$ respond to the capacitive contribution and the diffusion contribution, respectively. According to the CV measurements, the percentage of contribution is shown in Fig. 4c. With increased scan rates, the capacitive-controlled contribution of the $Ni_{0.75}Zn_{0.25}MoO_4$ electrode is 54, 63, 70, 76, 81, and 92% at 0.2, 0.4, 0.6, 0.8, 1, and 2 mV s^{-1} respectively. It can be noticed that when the scan rate is higher than 2 mV s^{-1}, the capacitive-controlled contribution almost entirely dominates, which is ascribed to enhanced reactivity and improved conductivity.

As shown in Fig. 4d, the cycling behaviors of the $Ni_{0.75}Zn_{0.25}MoO_4$ electrode were carried out at 10 A g^{-1}. Compared with the pristine $NiMoO_4$ electrode, the cycling performance of the $Ni_{0.75}Zn_{0.25}MoO_4$ electrode exhibits a significantly slower decrease in capacity retention during the initial several hundred cycles. We suggest that this is due to the improvement of crystallinity and the strength of the nanostructure during the cycling charge/discharge process. The specific capacitance retention of the $Ni_{0.75}Zn_{0.25}MoO_4$ electrode is ~40% after 600 cycles, while that of the $NiMoO_4$ electrode is 30%. The inset in Fig. 4d shows the GCD curves of the two electrodes before cycling. Longer discharge time obviously indicates the better performance of the $Ni_{0.75}Zn_{0.25}MoO_4$ electrode. In Fig. S7 (ESI†), the cycling stability of the obtained powder materials was also studied. The capacitance retention of the $NiMoO_4$ powder material quickly decreases while other Zn-doped materials still maintain a better stability. Furthermore, as shown in Fig. 4e, the SEM images after cycling indicate that its nanostructure is basically well preserved, and even the originally weak ultra-thin nanoflakes have become slightly stronger with a certain increase in thickness due to the volume changes during the charge and discharge cycles. From the above-mentioned cycling behaviors, it can be observed that it is an effective strategy to adjust the composition and crystal structure of the material *via* heteroatom doping to improve the cycling stability.

The performance of the obtained $Ni_{0.75}Zn_{0.25}MoO_4$ electrode was characterized in a two-electrode aqueous NiZn cell

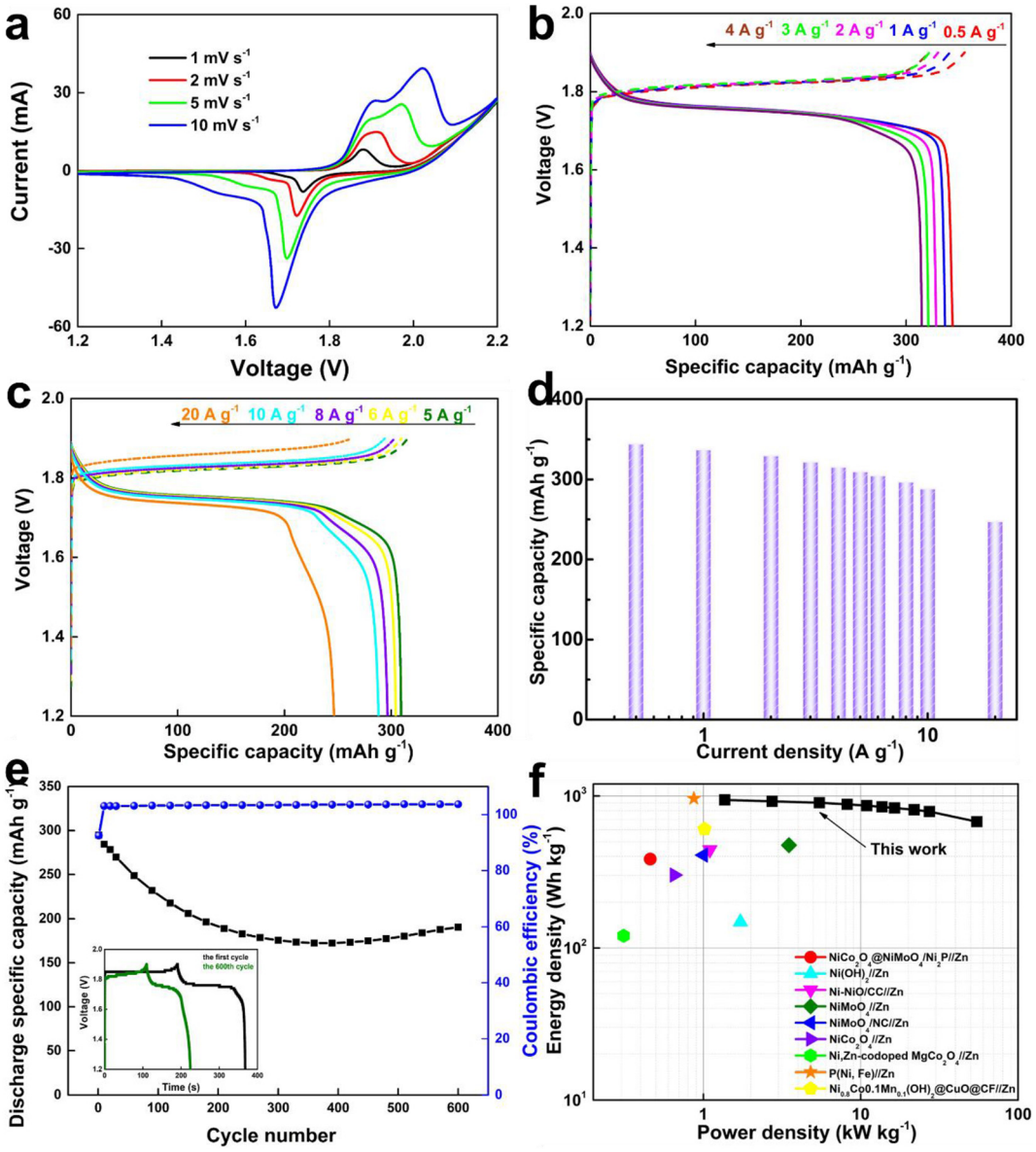

Fig. 5 $Ni_{0.75}Zn_{0.25}MoO_4$//Zn cell in a 6 M KOH electrolyte: (a) CV curves, (b and c) GCD curves, (d) specific capacities at different current densities, (e) cycling stability at 6 A g^{-1}, the inset shows the comparison of GCD curves before and after cycling, and (f) Ragone plots.

with a zinc counter electrode in a 6 M KOH solution. As shown in Fig. 5a, the CV curves of the $Ni_{0.75}Zn_{0.25}MoO_4$//Zn cell were measured within the voltage window of 1.2–2.2 V at different scan rates. The curves present a similar shape, without significant deformation with the gradual increase in scan rates, demonstrating fast reaction kinetics and good interface properties. In order to evaluate the energy storage performance of the assembled NiZn cell, the GCD curves at different current densities were tested, which are presented in Fig. 5b and c. All GCD curves show a stable charge/discharge platform and maintain good shapes, indicating its good rate performance and reversibility. Fig. 5d shows the discharge capacity of the $Ni_{0.75}Zn_{0.25}MoO_4$//Zn cell based on the activated material's mass of the $Ni_{0.75}Zn_{0.25}MoO_4$ electrode. The capacities are 344.7, 337.3, 330, 322, 315.5, 309.9, 304.8, 296.9, 288.5 and 247.6 mA h g^{-1} at current densities of 0.5, 1, 2, 3, 4, 5, 6, 8, 10 and 20 A g^{-1}, respectively.

Fig. 5e displays the cycling stability of the $Ni_{0.75}Zn_{0.25}MoO_4$//Zn cell, and the capacity retains 65% of the initial value with 100% of coulombic efficiency after 600 cycles at a high current density of 6 A g^{-1}. The Ragone plots in Fig. 5f show the energy density of the $Ni_{0.75}Zn_{0.25}MoO_4$//Zn cell to be 942.53 W h kg^{-1} at a power density of 1.37 kW kg^{-1}. When the power density of the NiZn cell reaches up to 54.69 kW kg^{-1}, the energy density still remains at 676.93 W h kg^{-1}, which surpasses those of previously reported aqueous NiZn batteries, such as $NiMoO_4$–NC//Zn (407.8 W h kg^{-1} at 18.1 kW kg^{-1}),[16] Ni $(OH)_2$//Zn (148.54 W h kg^{-1} at 1.72 kW kg^{-1}), Co-doped $NiMoO_4$//Zn (474.1 W h kg^{-1} at 3.5 kW kg^{-1}),[29] P(Ni, Fe)//Zn (962.6 W h kg^{-1} at 0.87 kW kg^{-1}),[35] $Ni_{0.8}Co_{0.1}Mn_{0.1}(OH)_2$@CuO@CF//Zn (605.2 W h kg^{-1} at 1.017 kW kg^{-1}),[42] Ni–NiO–CC//Zn (441.7 W h kg^{-1} at 1.1 kW kg^{-1}),[43] $NiCo_2O_4$@$NiMoO_4$/Ni_2P//Zn (384 W h kg^{-1} at 0.46 kW kg^{-1}),[18] $NiCo_2O_4$//Zn (301.3 W h kg^{-1} at 0.654 kW kg^{-1}),[44] and Ni,Zn-codoped $MgCo_2O_4$//Zn (120.4 W h kg^{-1} at 0.3119 kW kg^{-1}).[30]

4. Conclusions

In this work, $Ni_{1-x}Zn_xMoO_4$ nanoflakes have been synthesized by doping Zn into $NiMoO_4$ by a one-step hydrothermal method. Combining the advantages of unique nanoflake structures, improved conductivity, and tunable electronic interaction, the obtained $Ni_{0.75}Zn_{0.25}MoO_4$ electrode achieved an outstanding specific capacity of 345.84 mA h g^{-1} at 1 Ag^{-1}, good rate capability, and improved cycling stability. Furthermore, a NiZn cell was fabricated with the $Ni_{0.75}Zn_{0.25}MoO_4$ cathode and Zn anode, which presents a high discharge capacity of 344.7 mA h g^{-1} at 0.5 A g^{-1} and good cycling stability. Moreover, this battery displayed a high energy density of 942.53 W h kg^{-1} at a power density of 1.37 kW kg^{-1}, making it a promising candidate for aqueous rechargeable alkaline batteries. Additionally, this progress in the material design of Ni electrodes enabling high-performance energy storage may also be applied to other battery systems.

Author contributions

X. Y. Zhang – Conceptualization, data curation, project administration, and writing – original draft. D. Noréus – Supervision, and writing – review and editing.

Data availability

The data supporting this article have been included as part of the ESI.†

Conflicts of interest

The authors declare no competing financial interest.

Acknowledgements

This work was supported by the ÅForsk project (No. 23-411). The authors thank Prof. Jiayin Yuan for the electrochemical measurement platform.

References

1 H. Li, Z. Wang, L. Chen and X. Huang, *Adv. Mater.*, 2009, **21**, 4593–4607.
2 E. Goikolea, V. Palomares, S. J. Wang, I. R. de Larramendi, X. Guo, G. X. Wang and T. Rojo, *Adv. Energy Mater.*, 2020, **10**, 2002055.
3 M. Song, H. Tan, D. Chao and H. J. Fan, *Adv. Funct. Mater.*, 2018, **28**, 180256.
4 Y. Song, X. Lu, P. Deng, W. Hu, Z. Sun, X. X. Liu and X. Sun, *Chem. Eng. J.*, 2018, **354**, 672–679.
5 V. G. Lacerda, A. B. Mageste, I. J. B. Santos, L. H. M. da Silva and M. D. C. H. da Silva, *J. Power Sources*, 2009, **193**, 908–913.
6 J. O. G. Posada, A. J. R. Rennie, S. P. Villar, V. L. Martins, J. Marinaccio, A. Barnes, C. F. Glover, D. A. Worsley and P. J. Hall, *Renewable Sustainable Energy Rev.*, 2017, **68**, 1174–1182.
7 R. Wang, Y. Han, Z. Wang, J. Jiang, Y. Tong and X. Lu, *Adv. Funct. Mater.*, 2018, **28**, 1802157.
8 Y. Shi, Y. Chen, L. Shi, K. Wang, B. Wang, L. Li, Y. Ma, Y. Li, Z. Sun, W. Ali and S. Ding, *Small*, 2020, **16**, e2000730.
9 W. Shang, W. Yu, Y. Liu, R. Li, Y. Dai, C. Cheng, P. Tan and M. Ni, *Energy Storage Mater.*, 2020, **31**, 44–57.
10 H. Zhang, R. Wang, D. Lin, Y. Zeng and X. Lu, *ChemNanoMat*, 2018, **4**, 525–536.
11 E. Shangguan, H. Tang, Z. Chang, X. Z. Yuan and H. Wang, *Int. J. Hydrogen Energy*, 2011, **36**, 10057–10064.
12 L. Zhu, B. Fei, Y. Xie, D. Cai, Q. Chen and H. Zhan, *ACS Appl. Mater. Interfaces*, 2021, **13**, 22304–22313.
13 Y. Zeng, Y. Meng, Z. Lai, X. Zhang, M. Yu, P. Fang, M. Wu, Y. Tong and X. Lu, *Adv. Mater.*, 2017, **29**, 1702698.

14 Q. Chen, J. Li, C. Liao, G. Hu, Y. Fu, O. K. Asare, S. Shi, Z. Liu, L. Zhou and L. Mai, *J. Mater. Chem. A*, 2018, **6**, 19488–19494.
15 L. Li, R. Xiao, X. Tao, Y. Wu, L. Jiang, Z. Zhang and Y. Qing, *J. Power Sources*, 2021, **491**, 229618.
16 L. Zhou, S. Zeng, D. Zheng, Y. Zeng, F. Wang, W. Xu, J. Liu and X. Lu, *Chem. Eng. J.*, 2020, **400**, 125832.
17 W. Kang, Y. Sun, B. Xu, J. Li, X. Kong, D. Huang, X. Zhang, H. Yang and B. Lin, *Electrochim. Acta*, 2019, **323**, 134819.
18 Z. Cen, F. Yang, J. Wan and K. Xu, *New J. Chem.*, 2022, **46**, 6587–6595.
19 B. Jia, D. Zhu, S. Zhou, S. Luo, Z. Liu, B. Li and M. Liu, *Chem. Commun.*, 2023, **59**, 2950–2953.
20 Y. Jian, D. Wang, M. Huang, H. L. Jia, J. Sun, X. Song and M. Guan, *ACS Sustainable Chem. Eng.*, 2017, **5**, 6827–6834.
21 G. Zhang, H. Yang, H. Zhou, T. Huang, Y. Yang, G. Zhu, Y. Zhang and H. Pang, *Angew. Chem., Int. Ed.*, 2024, **63**, e202401903.
22 J. Tian, M. Peng, M. Luo, J. Lan, Y. Zhang and Y. Tan, *Small*, 2022, **18**, e2200452.
23 K. Wang, X. Fan, S. Chen, J. Deng, L. Zhang, M. Jing, J. Li, L. Gou, D. Li and Y. Ma, *Small*, 2023, **19**, e2206287.
24 X. Zhu, Y. Wu, Y. Lu, Y. Sun, Q. Wu, Y. Pang, Z. Shen and H. Chen, *J. Colloid Interface Sci.*, 2021, **587**, 693–702.
25 N. Wang, H. Liu, M. Sun, X. Ren, L. Hu, Z. Li, X. Yao, Y. Gong and C. Jia, *ACS Sustainable Chem. Eng.*, 2024, **12**, 3527–3537.
26 M. Liang, X. Li, Y. Kang, N. U. RehmanLashari, X. Zhang, Y. Zhao, H. Wang, Z. Miao and C. Fu, *J. Power Sources*, 2022, **535**, 231486.
27 Y. Pang, L. Li, Y. Wang, X. Zhu, J. Ge, H. Tang, Y. Zheng, F. Wang, S. Wu, Q. Wu, Z. Shen and H. Chen, *Chem. Eng. J.*, 2022, **436**, 135202.
28 X. Liang, X. Zou, X. Ren, B. Xiang, W. Li, F. Chen, J. Hao, Q. Hu and L. Feng, *J. Colloid Interface Sci.*, 2020, **578**, 677–684.
29 Y. Shen, K. Zhang, F. Yang, Z. Li, Z. Cui, R. Zou, Q. Liu, J. Hu and K. Xu, *Sci. China Mater.*, 2020, **63**, 1205–1215.
30 Z. Zhu, R. Zhang, J. Lin, K. Zhang, N. Li, C. Zhao, G. Chen and C. Zhao, *J. Power Sources*, 2019, **437**, 226941.
31 S. Wang, X. Duan, T. Gao, Z. Wang, D. Zhou, K. Sun, Z. Shang, Y. Kuang, S. Tian, X. Li, W. Liu and X. Sun, *J. Electrochem. Soc.*, 2020, **167**, 160550.
32 B. Huang, D. Yao, J. Yuan, Y. Tao, Y. Yin, G. He and H. Chen, *J. Colloid Interface Sci.*, 2022, **606**, 1652–1661.
33 M. P. Dabir, S. M. Masoudpanah and M. Mamizadeh, *J. Energy Storage*, 2024, **76**, 109826.
34 X. Zhang, Z. Li, Z. Yu, L. Wei and X. Guo, *Appl. Surf. Sci.*, 2020, **505**, 144513.
35 X. Zhang, Y. Liu and D. Noréus, *ACS Appl. Energy Mater.*, 2024, **7**, 517–527.
36 A. S. Keshari and P. Dubey, *J. Energy Storage*, 2021, **40**, 102629.
37 D. Aman, S. Abdel-Azim, S. Said and S. G. Mohamed, *RSC Adv.*, 2022, **12**, 7120–7132.
38 X. Zhang, L. Wei and X. Guo, *Chem. Eng. J.*, 2018, **353**, 615–625.
39 T. Liu, H. Chai, D. Jia, Y. Su, T. Wang and W. Zhou, *Electrochim. Acta*, 2015, **180**, 998–1006.
40 X. Zhang, E. A. Toledo-Carrillo, D. Yu and J. Dutta, *ACS Appl. Mater. Interfaces*, 2022, **14**, 40371–40381.
41 M. Forghani and S. W. Donne, *J. Electrochem. Soc.*, 2018, **165**, A664–A673.
42 Y. Yu, J. Liu, Y. Zhang, K. Song, X. Hu, Y. Zhu and X. Hu, *J. Alloys Compd.*, 2022, **908**, 164704.
43 L. Li, L. Jiang, Y. Qing, Y. Zeng, Z. Zhang, L. Xiao, X. Lu and Y. Wu, *J. Mater. Chem. A*, 2020, **8**, 565–572.
44 W. Shang, W. Yu, P. Tan, B. Chen, H. Xu and M. Ni, *J. Power Sources*, 2019, **421**, 6–13.